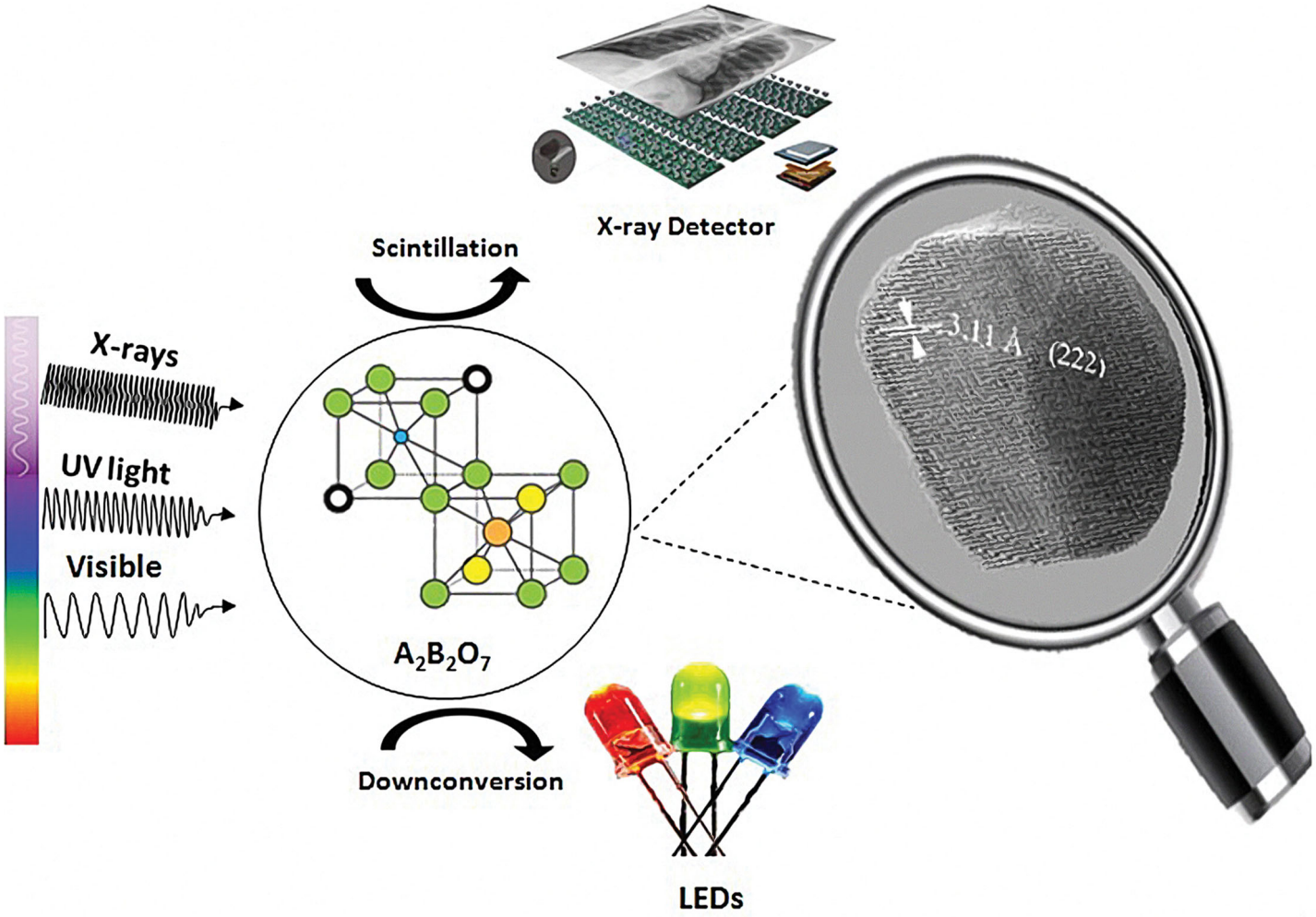

Highlighting research conducted by J. P. Zuniga *et al.* from the Multifunctionalized Applications of Oxides (MAO) Research Group at the Department of Chemistry, University of Texas Rio Grande Valley, United States

Exploring the optical properties of $La_2Hf_2O_7:Pr^{3+}$ nanoparticles under UV and X-ray excitation for potential lighting and scintillating applications

Nanomaterials have received intensive attention due to their unique properties. Here complex metal oxide nanoparticles activated by lanthanide ions were prepared by the molten salt synthesis method. They demonstrated superior emission and scintillation performance for various potential applications.

As featured in:

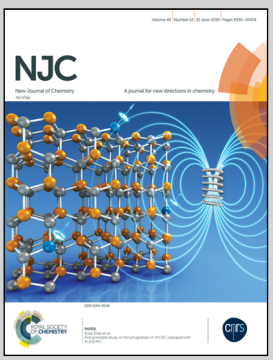

See Yuanbing Mao *et al.*, *New J. Chem.*, 2018, **42**, 9381.

ROYAL SOCIETY OF CHEMISTRY

rsc.li/njc

Registered charity number: 207890

NJC

PAPER

View Article Online
View Journal | View Issue

Cite this: *New J. Chem.*, 2018, 42, 9381

Exploring the optical properties of $La_2Hf_2O_7:Pr^{3+}$ nanoparticles under UV and X-ray excitation for potential lighting and scintillating applications†

Jose P. Zuniga,[a] Santosh K. Gupta,[ab] Madhab Pokhrel[ac] and Yuanbing Mao *[ad]

New optical materials with efficient luminescence and scintillation properties have drawn a great deal of attention due to the demand for optoelectronic devices and medical theranostics. Their nanomaterials are expected to reduce the cost while incrementing the efficiency for potential lighting and scintillator applications. In this study, we have developed praseodymium-doped lanthanum hafnate ($La_2Hf_2O_7:Pr^{3+}$) pyrochlore nanoparticles (NPs) using a combined co-precipitation and relatively low-temperature molten salt synthesis procedure. XRD and Raman investigations confirmed ordered pyrochlore phase for the as-synthesized undoped and Pr^{3+}-doped $La_2Hf_2O_7$ NPs. The emission profile displayed the involvement of both the $^3P_0$ and $^1D_2$ states in the photoluminescence process, however, the intensity of the emission from the $^1D_2$ states was found to be higher than that from the $^3P_0$ states. This can have a huge implication on the design of novel red phosphors for possible application in solid-state lighting. As a function of the Pr^{3+} concentration, we found that the 0.1%Pr^{3+} doped $La_2Hf_2O_7$ NPs possessed the strongest emission intensity with a quantum yield of 20.54 ± 0.1%. The concentration quenching, in this case, is mainly induced by the cross-relaxation process $^3P_0 + {}^3H_4 \rightarrow {}^1D_2 + {}^3H_6$. Emission kinetics studies showed that the fast decaying species arise because of the Pr^{3+} ions occupying the Hf^{4+} sites, whereas the slow decaying species can be attributed to the Pr^{3+} ions occupying the La^{3+} sites in the pyrochlore structure of $La_2Hf_2O_7$. X-ray excited luminescence (XEL) showed a strong red-light emission, which showed that the material is a promising scintillator for radiation detection. In addition, the photon counts were found to be much higher when the NPs are exposed to X-rays when compared to ultraviolet light. Altogether, these $La_2Hf_2O_7:Pr^{3+}$ NPs have great potential as a good down-conversion phosphor as well as scintillator material.

Received 21st February 2018,
Accepted 7th April 2018

DOI: 10.1039/c8nj00895g

rsc.li/njc

1. Introduction

Apart from numerous applications in various advanced fields such as light emitting diodes,[1] laser,[2] biomedicine,[3] catalysis,[4] and solar cells,[5] lanthanide ion doped phosphor materials can also be used as scintillators or dosimeters depending upon the applications and processes involved.[6] Scintillation materials are also used for various applications ranging from photodynamic therapy,[7] security,[8] well-logging,[9] medical imaging,[10] *etc.* Research based on exploring novel scintillator materials is one field that is receiving a large amount of attention over the last ten years and the search for rapid and efficient materials for such applications is always going to be the main research area in this particular field. The process of scintillation is a type of radioluminescence (RL) in which high-energy photons are absorbed and finally lead to an emission of light. It typically consists of three different steps: (i) Incoming radiation is converted into a large number of electron–hole (e^-–h^+) pairs, (ii) energy transfer from the e^-–h^+ pairs to the luminescent active ions, and (iii) radiative emission due to de-excitation of the luminophores from an excited state to the ground state. Scintillators are usually considered best if they possess various favorable properties such as high density, effective *Z*-number, emission output, energy resolution and radiation hardness in addition to being easy to grow in large quantities at low cost.[11]

The systems comprised of the $Ln_2M_2O_7$ composition (Ln: trivalent lanthanides and M: tetravalent titanium group

[a] *Department of Chemistry, University of Texas Rio Grande Valley, 1201 West University Drive, Edinburg, Texas 78539, USA. E-mail: yuanbing.mao@utrgv.edu; Tel: +1-956-665-2986*
[b] *Radiochemistry Division, Bhabha Atomic Research Center, Mumbai, 400085, India*
[c] *Department of Physics, University of Texas Rio Grande Valley, 1201 West University Drive, Edinburg, Texas 78539, USA*
[d] *School of Earth, Environmental, and Marine Sciences, University of Texas Rio Grande Valley, 1201 West University Drive, Edinburg, Texas 78539, USA*

† Electronic supplementary information (ESI) available. See DOI: 10.1039/c8nj00895g

elements, such as Ti, Zr and Hf) have been explored extensively because of their various scientific and technological importance in various areas such as gas sensors,[12] thermal barrier coatings,[13] solid oxide fuel cells,[14] neutron absorbing materials[15] and nuclear waste hosts.[16] The structure plays a very crucial role for all the applications mentioned above and these compounds are known to exist as two structural variants, ordered pyrochlore and disordered fluorite structures, each having specific applications. A cubic pyrochlore structure is preferred and is more suited for scintillator materials because the oxygen vacancies are well distributed through the lattice of the hosts giving a sense of symmetry to the overall structure and therefore, sintering them into transparent ceramic will be easier.[17] On the other hand, the cubic defect fluorite structure has a random distribution of oxygen vacancies in the structure, which is not suitable for scintillators.[18] A phase transition can be induced chemically by doping or applying higher temperature and pressure. The phase transformation from ordered pyrochlore to defect fluorite involves the randomization of the oxygen ions among the 48f, 8b, and 8a sites, and the cations between the 16c and 16d sites.[19] Among the various pyrochlores, $La_2Hf_2O_7$, lanthanum hafnate, stands out as a material with special properties for optical applications. $La_2Hf_2O_7$ offers a set of properties that make it very attractive for novel high-energy radiation detectors. These properties include high stopping power for X- and γ-rays with Z_{Hf} = 72 and a high density of 7.9 g cm^{-3}.[17,18] Despite their various favorable properties, hafnate pyrochlores have not been given due credit when compared to their titanate and zirconate counterparts. Our group[19] have investigated the photoluminescence (PL) and RL properties of $La_2Hf_2O_7$:Eu^{3+} whereas Hansel *et al.*[20] have explored the same material for non-contact thermometry. We have also carried out systematic studies on the structural and optical properties of various Eu^{3+}-doped rare earth (RE) hafnates $RE_2Hf_2O_7$ (RE = Y, La, Pr, Gd, Er, and Lu) nanoparticles (NPs).[21] The interest in the Pr^{3+} intra-configurational (f-f) and inter-configurational (f-d) emission arises from their possible potential applications in solid state lighting, display devices, medical, and security industries.[22] Hosts such as $La_2Hf_2O_7$ are expected to yield good radioluminescence upon doping with Pr^{3+} due to its favorable properties mentioned above, specifically its high stopping power for X-ray and γ-rays and high density. As far as dopant ions are concerned, we wanted to investigate the materials characteristics and the optical and scintillation properties of trivalent praseodymium ion-doped $La_2Hf_2O_7$.

Furthermore, Pr^{3+} is a unique lanthanide ion as it emits in the visible-light as well as near-infrared regions of the electromagnetic spectrum. It is frequently used as an optical component for solid, state based lighting in view of its ability to exhibit an up-conversion process, wherein blue light is emitted from the $^3P_0$ level upon multiple photon pumping in the $^1G_4$ or $^1D_2$ levels.[23] There are few works on exploring $La_2Hf_2O_7$ for scintillator applications with dopants such as cerium(III)[24] and titanium(IV).[25] It is also unique in a way that both trivalent and tetravalent dopants can be localized in the Ln^{3+}- and M^{4+}-sites of the $Ln_2M_2O_7$ systems, respectively. Trojan-Piegza *et al.*[18,26] have explored the PL and RL properties of $La_2Hf_2O_7$:Pr^{3+} NPs synthesized using a Pechini sol–gel method. In one case, they recorded the PL and RL of their NPs after being annealed at 1000 and 1400 °C, respectively.[18,26] In another case, they compared the PL and RL properties of the powder and ceramic forms.[18,26] The structural analysis in these papers were performed using X-ray diffraction (XRD) only. X-rays are scattered by electrons, so the high atomic number elements including Ln and Hf are stronger scatterers of X-rays when compared to oxygen atoms. Therefore, X-ray fails to give information pertaining to the oxygen ions. This information is very important if one needs to explore pyrochlore-based materials for various optical, electrical and other technological applications. Sometimes, it is even very difficult to distinguish a completely disordered pyrochlore phase from a fluorite compound using XRD. Considering the reconstructive nature of the transition of these two phases, there may also be the chance that these two phases may co-exist at some point. In this sense, other techniques such as Raman and Fourier-transform infrared (FTIR) spectroscopy are advantageous over X-ray diffraction. FTIR is employed to confirm the purity of the samples and presence of metal–oxygen vibrational modes whereas Raman spectroscopy is carried out to probe the local disorder and purity of the synthesized phase. Raman spectroscopy is a highly sensitive technique used to probe metal–oxygen vibrations and hence a very good probe for studying the local disorder in materials.[27] It has been observed in some cases that Raman spectroscopy can provide highly reliable information in regard to distinguishing defect fluorite and pyrochlore structures.[28]

In this study, we aimed to explore the efficiency of $La_2Hf_2O_7$:Pr^{3+} NPs as a potential candidate material for use in lighting and scintillators materials. Therefore, we have synthesized $La_2Hf_2O_7$ NPs with various Pr^{3+} doping concentrations using a combined co-precipitation and relatively low temperature molten salt method. We have extensively used of Raman and FTIR spectroscopy, and X-ray photoemission spectroscopy (XPS) for our structural, oxidation state and elemental composition studies. In addition, the synthesized NPs were characterized using transmission electron microscopy (TEM) and scanning electron microscopy (SEM) to visualize their size and morphology. Moreover, to evaluate their PL and RL properties steady-state luminescence and time-resolved PL spectroscopy (TRPLS) was performed exploiting both ultraviolet and X-ray radiation. Furthermore, we have performed RL and photon count measurements for X-rays and the PL as a function of dopant concentration while optimizing the X-ray excitation power to yield the maximum photon count for our quantum yield studies. Based on the best of our knowledge, the current study is the most complete report on the optical properties of $La_2Hf_2O_7$:*x*mol%Pr^{3+} NPs under both UV and X-ray excitation.

2. Experimental

2.1 Synthesis methods

All chemicals used in this study are analytical grade reagents (AR grade) and were used without any further purification. The starting materials used for the synthesis of the $La_2Hf_2O_7$:Pr^{3+}

are as follows: Lanthanum nitrate hexahydrate ($La(NO_3)_3{\cdot}6H_2O$, 99.0%), hafnium dichloride oxide octahydrate ($HfOCl_2{\cdot}8H_2O$, 99.0%), praseodymium(III) nitrate hexahydrate ($Pr(NO_3)_3{\cdot}6H_2O$, 99.9%), potassium nitrate (KNO_3, 99.9%), sodium nitrate ($NaNO_3$, 98%) and ammonium hydroxide (NH_4OH, 28.0–30.0%). The $La_2Hf_2O_7$:*x*mol%Pr^{3+} NPs (x = 0.0, 0.1, 0.2, 0.3, 0.5, and 1.0) were prepared using a two-step molten salt process, which generates nanoparticles at a relatively low temperature as reported by our group and some other groups, for example in the synthesis of YAG:Ce and LuAG:Ce.[19,21,29–31] First, a single-source precursor was prepared by measuring $(5 - x)$ mmol of $La(NO_3)_3{\cdot}6H_2O$ and 5 mmol of $HfOCl_2{\cdot}8H_2O$ and x mmol of $Pr(NO_3)_3{\cdot}6H_2O$, where x is equal to the mol% with respect to the La^{3+} sites. The materials were dissolved in 200 mL of 18.2 mΩ Millipore water while simultaneously stirred with a magnetic stirring rod. A titration was set up using 10% diluted ammonium as the titrant, which was delivered into the metal solution dropwise over a period of 2 h. The white precipitate formed was collected by vacuum filtration and washed with DI water until neutral pH. In the next step, the molten salt method was used to ensure the size-controlled synthesis of $La_2Hf_2O_7$:*x*mol%Pr^{3+} NPs *via* a flux. Specifically, the single-source precursor was mixed with nitrate salts ($NaNO_3$ and KNO_3 in 1 : 1 molar ratio) and placed in a furnace at 650 °C for 6 h followed by washing with 18.2 mΩ Millipore water and drying. The molten salt method is of particular of interest because it allows for the formation of pure products, even nanoparticles, at relatively low temperatures when compared to conventional solid-state or sol–gel methods by forming a flux around the precursor when the salts reach an eutectic point allowing controlled crystal growth and therefore, particle size. In addition, the molten salt method ensures no phase transformations occur due to the low synthesis temperature and allows morphological tunability by controlling the cooling process.[31,32] In this study, the nanoparticle samples were later annealed for 1 h at 900 °C to optimize their optical properties.

2.2 Characterization

Several characterization methods were carried out on the as-synthesized $La_2Hf_2O_7$:*x*mol%Pr^{3+} NPs. XRD was performed to identify the purity of the as-synthesized NPs on a BRUKER™ D8 Advance X-ray diffractometer with Cu $K_{\alpha 1}$ radiation (λ = 1.5406 Å, 40 kV, 40 mA). The output data were collected in scanning mode in the 2θ range from 10° to 75° with a scanning step size of 0.04° at a scan rate of 2.0° min^{-1}. In addition, SEM was used to record the morphology of the as-synthesized NPs using a Carl Zeiss sigma VP field emission scanning electron microscope operated at 5 kV. Furthermore, energy dispersive X-ray (EDX) spectral mapping analysis was performed under 25 kV to record the composition of the NPs. To further confirm the crystal phase of the as-synthesized NPs, the Raman spectra were collected from their powdered form, using a Bruker Senterra-system with a 785 nm helium–neon laser at a spatial resolution of 2 μm. FTIR spectroscopy was used to identify the metal to oxygen vibrational modes of the NPs on a Thermo Nicolet Nexus™ 470 FT-IR system. XPS was obtained with a 180° double focusing hemispherical analyzer with a 128-channel detector using non-monochromatic Al Kα radiation (1486.86 eV) with a power of 240 W (Thermo Scientific™ K-Alpha™ X-ray photoelectron spectrometer system). This X-ray source was chosen to minimize the effects of the superposition of the photoelectrons and Auger lines of the constituent elements. The diameter of the X-ray beam was ~0.4 mm. The energy resolution of the instrument was chosen to be 0.73 eV in order to have a sufficiently small broadening of the natural core level lines together with a reasonable signal-to-noise ratio. The binding energy scale was calibrated with reference to Cu $3p_{3/2}$ (75.1 eV) and Cu $2p_{3/2}$ (932.7 eV) lines, giving an accuracy of 0.1 eV in any peak energy position determination.

The excitation, emission and lifetime spectra were measured using an Edinburgh Instruments FLS 980 fluorometer system equipped with both a steady state source as well as a pulsed source with a frequency range of 1–100 Hz. Lastly, the RL was acquired by designing a silver target (λ = 0.52 Å, 60 kV, 200 mA) X-ray tube adaptor for the FLS 980 fluorometer system. Copper metal was used to dissipate heat around the tube using a half inch-thick sheet. In addition, an X-ray guide set-up was constructed to prevent the X-ray beam from scattering and to focus on the sample. Protective equipment was constructed to protect the user from radiation using a 0.75 mm thick lead curtain on a rail to surround the instrument. Additional lead was used in the form of sheets to cover the top of the instrument.

3. Results and discussion

3.1 The phase purity and crystallite size of the $La_2Hf_2O_7$:*x*mol%Pr^{3+} NPs: X-ray diffraction

Fig. 1a shows the XRD patterns of the $La_2Hf_2O_7$:*x*mol%Pr^{3+} (x = 0.1, 0.2, 0.3, 0.5, and 1.0) NPs. The peaks presented in the XRD data are well defined, sharp, and intense in nature indicating the high crystalline nature of the as-synthesized NPs. The peak position confirms the fact that the as-synthesized $La_2Hf_2O_7$:Pr^{3+} NPs were stabilized in the cubic fluorite phase with the peaks indexed to the (222), (400), (440), and (662) planes. Due to the insensitivity of XRD to the superlattice reflections of the pyrochlore phase at (311), (331), (511), and (531) (corresponding to the 2θ values of 27°, 36°, 43°, and 50°, respectively), we indexed the XRD peaks to the fluorite phase for the moment while Raman spectroscopy was used to identify their structure differently.[19] In addition, Fig. 1b shows the variation in the XRD peak positions corresponding to the most intense (222) peak at 2θ between 28 to 29° as the function of the Pr^{3+} dopant concentration. Furthermore, the lattice parameter a was calculated using Braggs equation with the (hkl) plane equation to confirm the consistency of the XRD data based on the (222) XRD peak shown in Fig. 1b. The particle size of the as-synthesized NPs was calculated using Scherrer's equation using the full width half max (FWHM) of the (222) plane. The lattice parameters of the $La_2Hf_2O_7$:*x*mol%Pr^{3+} (x = 0.1, 0.2, 0.3, 0.5, and 1.0) NPs are tabulated in Table 1. The crystallite size of the NPs obtained from all the doping levels is in nano-size domain. The calculated crystallite sizes are in agreement with both the SEM and TEM data presented in Fig. 3.

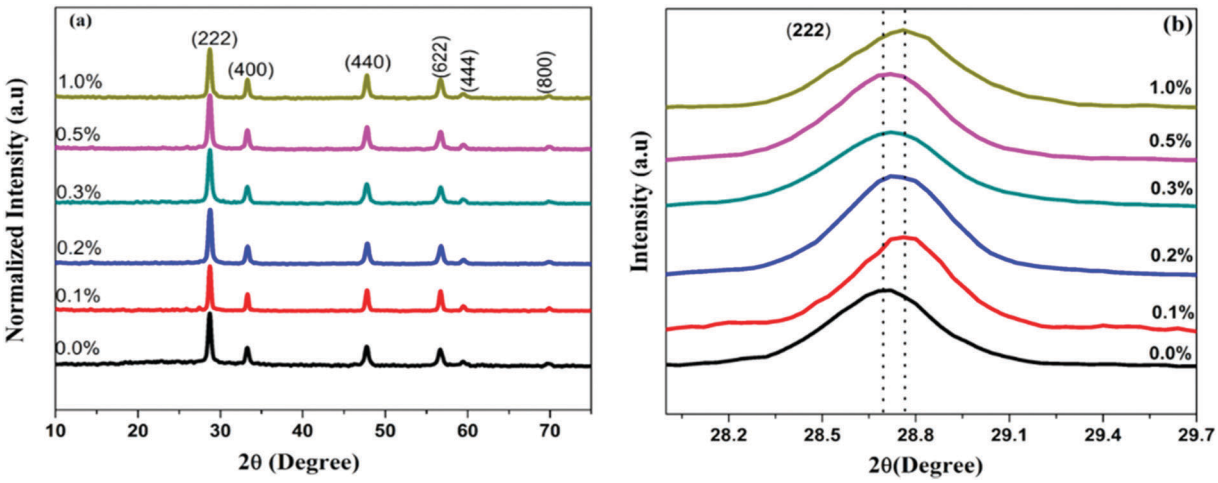

Fig. 1 (a) The XRD patterns and (b) enlarged view of the XRD peak corresponding to the (222) plane at ~28.72° of the $La_2Hf_2O_7$:x mol%Pr^{3+} NPs (x = 0, 0.1, 0.2, 0.3, 0.5, and 1.0) calcined at 900 °C.

Table 1 The lattice parameters of the $La_2Hf_2O_7$:x mol%Pr^{3+} NPs as a function of the dopant concentration (x = 0, 0.1, 0.2, 0.3, 0.5, and 1.0)

Pr^{3+} doping concentration (%)	2θ (°)	FWHM (β)	Lattice parameters (Å)
0.00	28.69	0.24	10.77
0.10	28.72	0.11	10.76
0.20	28.73	0.20	10.75
0.30	28.71	0.26	10.76
0.50	28.70	0.21	10.76
1.00	28.71	0.22	10.76

In general, the solid solutions follow Vegard's law with the linearity of lattice parameter in accordance with the ionic size of dopant ion and its concentration.[33] From Table 1, it can be easily seen that there is little change in the lattice parameters of the NPs upon increasing the Pr^{3+} concentration from 0.1 to 1.0 mol% because of the similar radii of La^{3+} and Pr^{3+} ions and the low Pr^{3+} doping level.

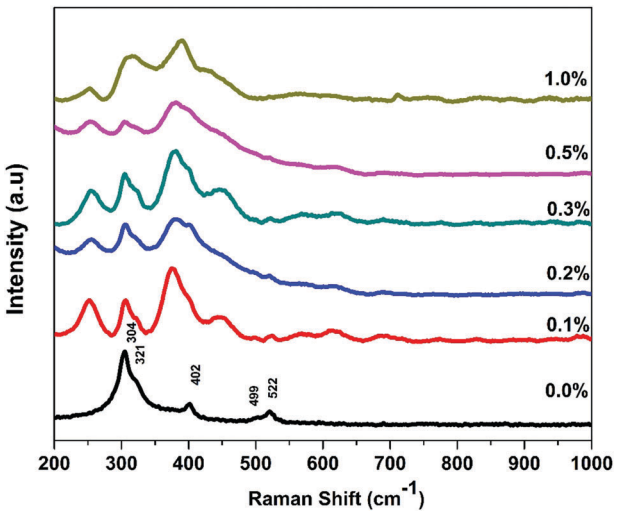

Fig. 2 The Raman spectra of the $La_2Hf_2O_7$:x mol%Pr^{3+} (x = 0, 0.1, 0.2, 0.3, 0.5, and 1.0) NPs calcined at 900 °C.

3.2 Raman analysis

In the literature, it is well known that the cubic pyrochlore structure processes a total of six Raman active modes, which according to group theory are $\Gamma = A_{1g} + E_g + 4F_{2g}$,[34,35] while the defect fluorite structure has only one active mode, F_{2g}. The Raman spectrum of fluorite phase mainly displays a single broad peak because the seven O^{2-} ions are randomly distributed over the 8 anionic sites in this structure giving rise to significant disorder. In Fig. 2, for pure $La_2Hf_2O_7$ we could clearly identify five Raman active modes pertaining to the vibrations of the Ln–O and Hf–O bonds at around 304, 321, 402, 499, and 522 cm^{-1}, which are assigned to F_{2g}, E_g, F_{2g}, F_{2g}, and A_{1g}, respectively.[36] The sixth Raman mode at 600 cm^{-1} (F_{2g} band) is not observed in our samples, as it is often reported that this particular band is absent in many pyrochlores.[37] The vibrational modes in the lower frequency region (300–400 cm^{-1}), *i.e.* the F_{2g}, E_g, and F_{2g} modes, arise from the vibrations of the La–O and Hf–O bonds. On the other hand, the higher frequency band (522 cm^{-1}) of A_{1g} arise due to the stretching of the Hf–O bonds while the small kink around 710 cm^{-1} is ascribed to the distortion of the HfO_6 octahedral.[36] The acquired Raman spectra suggest that the crystal phase of the as-synthesized $La_2Hf_2O_7$:x mol%Pr^{3+} NPs is indeed in the pyrochlore phase and not in the defect fluorite structure, as suggested by the XRD data. The pyrochlore structure of the $A_2M_2O_6O'$ composition is composed of two varieties of chemical bonds, where the M–O bonds are relatively covalent and the A–O bonds are much weaker. The strongest band is located at 304 cm^{-1}, which can be attributed to the F_{2g} internal La–O stretching mode. The presence of the Raman band at ~260 cm^{-1} can be ascribed to two reasons: (i) doping induced peak splitting of the F_{2g} band at 304 cm^{-1} and (ii) the A_g translatory mode of Pr–O bond. According to Hooke's law, the vibrational frequency is inversely proportional to the effective mass. Since Pr is heavier than La, the vibration of the Pr–O bond is at lower wavenumber when compared to the La–O bond.

The bond length of Pr–O is actually longer than that of La–O, which causes the distance of oscillation to increase and therefore, the energy and wavenumber to decrease. The peak at 402 cm^{-1} is red-shifted to 374 cm^{-1} and may also be attributed to doping effect wherein the vibration of Pr–O interferes with the La–O bond vibration causing the Raman band to split and shift. The blue-shift is the result of the higher effective mass of Pr–O than La–O.[38] Overall, the use of Raman spectroscopy confirmed that the as-synthesized $La_2Hf_2O_7$:*x*mol%Pr^{3+} NPs possess the pyrochlore structure, a phase that is essential for the explored applications.

3.3 Infrared spectroscopy

FTIR spectroscopy was used to confirm the composition of the $La_2Hf_2O_7$:*x*mol%Pr^{3+} NPs in which the ratio of the pellet made for analysis was 1 : 10 in weight of the $La_2Hf_2O_7$:*x*mol%Pr^{3+} sample to KBr (Fig. S1, ESI†). Pyrochlore oxides ($A_2B_2O_7$) are known to possess seven IR active modes in the range of 750–50 cm^{-1} originating from vibration and bending of the A–O and B–O bonds.[39] The IR band (ν_1) at around 623 cm^{-1} is attributed to Hf^{IV}–O stretching mode in the HfO_6 octahedron and the second band (ν_2) around 519 cm^{-1} is attributed to La^{III}–O stretching mode. In addition, the inset of Fig. S1 (ESI†) shows the full range in which the data was collected, proving the absence of peaks corresponding to the hydroxyl, nitrogen, or inorganic salts used during the molten salt synthesis, showing the purity of the $La_2Hf_2O_7$:*x*mol%Pr^{3+} NPs after calcination. Upon doping Pr^{3+} ions into the $La_2Hf_2O_7$ NPs we could not find much difference in the FTIR spectral pattern, suggesting all the samples had a similar composition.

3.4 XPS analysis

XPS can be used to determine the chemical state/oxidation state of the elements and the surface composition of the annealed samples. Fig. S2 (ESI†) depicts the XPS spectra of La 3d, Hf 4f, O 1s, and Pr 3d of the $La_2Hf_2O_7$:*x*mol%Pr^{3+} NPs. The La 3d XPS spectra of the NPs and the binding energies (BE) of La $3d_{5/2}$ and La $3d_{3/2}$ at 837 and 854 eV in addition to the 841 and 858 eV La 3d satellite peaks are presented in Fig. S2a (ESI†). The La 3d X-ray photoelectron peak not only splits into $3d_{5/2}$ and $3d_{3/2}$ due to a spin–orbit coupling but additionally, each of these lines splits further due to a transfer of electrons from the oxygen ligands to the La 4f orbital.[40] The difference in the energy between the $3d_{3/2}$ and $3d_{5/2}$ states is approximately 17 eV. The BE value and the XPS peak splitting agree well with reported values obtained for La^{3+} compounds, which confirms the 3+ oxidation state of the lanthanum ions in our NPs.[41,42] Upon doping the Pr^{3+} ions, it can be seen that both peaks shift to higher BE values, which can be attributed to different chemical environment around the La^{3+} ions. On the other hand, most reports[43–45] depict a clear splitting of the Hf 4f peak to $4f_{7/2}$ and $4f_{5/2}$ similar to our observation. Fitting the curves of the Hf 4f core levels (Fig. S2b, ESI†) shows two typical peaks in pure $La_2Hf_2O_7$ at BE = 17.18 and 19.07 eV, corresponding to $4f_{5/2}$ and $^4f_{7/2}$, respectively with the 4f spin–orbit splitting energy calculated to be ~1.89 eV. The Hf $4f_{7/2}$ peak at BE = 19.07 eV indicates the formation of Hf–O bonds and the Hf^{4+} oxidation number. As a function of the dopant ion concentration, this doublet of the Hf–4f peaks shifts towards a higher BE value and the shift increases upon increasing the Pr^{3+} concentration. When compare to La 3d, the increase in the shift is more obvious because the bond length of La–O is greater than that of Hf–O in $La_2Hf_2O_7$.

Furthermore, the standard BE value from the photoelectrons of Pr $3d_{5/2}$ in the elementary substance is 931.9 eV (±0.1 eV) and in Pr_2O_3 is 933.2 eV (±0.1 eV),[46] which is very different from the experimental data in this study with an observed BE value of 938 eV (Fig. S2c, ESI†). The large shift in the BE values indicate the formation of Pr–O–La/Hf clusters in the $La_2Hf_2O_7$:*x*mol%Pr^{3+} NPs. Due to lower electronegativity of Pr compared to La, the electron cloud around Pr is much closer to oxygen in the Pr–O–La bond than the electron cloud from La, which results in the higher binding energy component of Pr in our samples when compared to that of Pr in Pr_2O_3 at 933.4 eV.

In addition, it is well known that the oxygen ions and oxygen vacancies are distributed across all the anion sub-lattice sites in $Ln_2M_2O_7$ compounds. With the addition of Pr^{3+} to the host it can be observed that both the oxygen ions and vacancies are rearranged or destroyed through the lattice. It can be observed from Fig. S2d (ESI†) that the undoped $La_2Hf_2O_7$ has binding energies of ~530.0 and 531.85 eV, which shift towards higher BE values in the $La_2Hf_2O_7$:*x*mol%Pr^{3+} NPs upon increasing the doping percentage of Pr^{3+}. In general, the O 1s profile is more complex due to the overlapping contribution of oxygen from La and Hf. Six out of every seven oxygen ions occupy the 48f sites and each is coordinated by two lanthanum and two hafnium ions, and the seventh oxygen ion occupies the 8b site and is surrounded by four hafnium ions. This means that the electron density on oxygen for the La–O bond is higher than that of the Hf–O bond, which could be the most possible reason for the observation of two binding energy peaks for O 1s in the $La_2Hf_2O_7$:0.1%Pr^{3+} crystal structure.[47] The O1s spectra is clean indicating that nitrogen is not present after the molten salt synthesis. In fact, if nitrogen was present, the oxygen peaks from the N–O bond would be present. Overall, the broadness of the peaks indicate that oxygen is distributed uniformly throughout the lattice structure.

3.5 Morphological study: scanning and transmission electron microscopies

SEM images of the undoped and Pr^{3+}-doped $La_2Hf_2O_7$ NPs annealed at 900 °C are shown in Fig. 3a–f. The undoped as well as Pr^{3+}-doped $La_2Hf_2O_7$ NPs are spherical in shape and monodisperse at a low doping level. The morphology of the NPs does not seem to vary too much as a function of the dopant ion concentration. At the highest doping concentration, the distribution reveals slight agglomeration, which still needs to be confirmed (Fig. 3f). The average size of the particles is 25–50 nm for most of the samples. A TEM study was carried on the $La_2Hf_2O_7$:1.0%Pr^{3+} NPs with the maximum Pr^{3+} doping concentration to see whether indeed any agglomeration existed in the sample (Fig. 3g). The observed monodisperse NPs

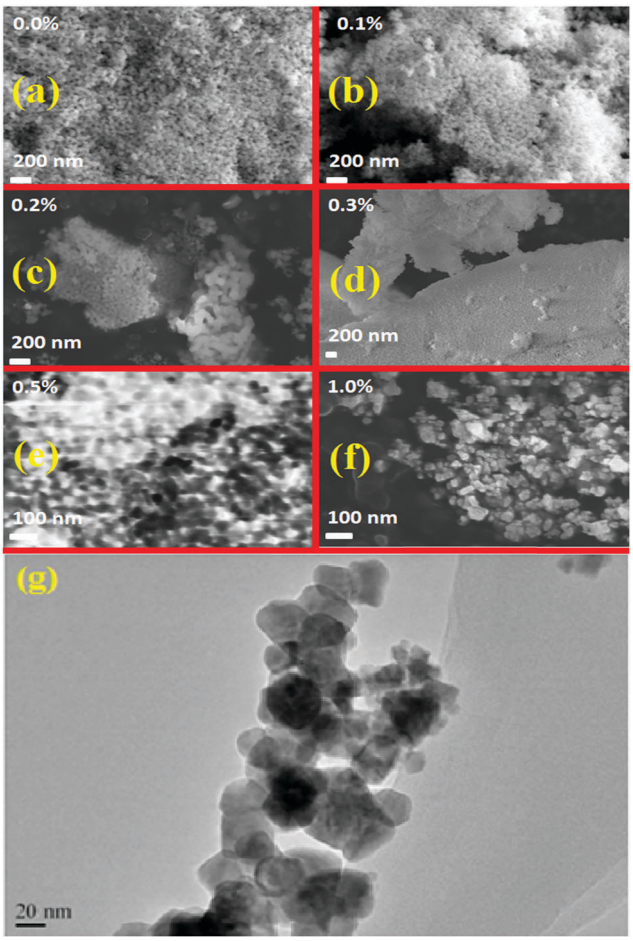

Fig. 3 (a–f) The SEM images of the $La_2Hf_2O_7$:xmol%Pr^{3+} (*x* = 0, 0.1, 0.2, 0.3, 0.5, and 1.0) NPs. (g) The TEM images of the $La_2Hf_2O_7$:1.0%Pr^{3+} NPs.

confirmed the advantage of our combined co-precipitation and molten salt synthesis procedure. Lastly, TEM also depicted that particles are more or less spherical in nature and the particle size is around 35 nm, which is in close agreement with the calculated size from the XRD data (Fig. 1).

3.6 Photoluminescence: optical properties under UV excitation

PL studies were carried out to understand the excitation, emission and lifetime decay of the $La_2Hf_2O_7$:Pr^{3+} NPs. Fig. 4a shows the excitation spectra of the $La_2Hf_2O_7$:Pr^{3+} NPs displaying features, which are characteristic of the 4f–5d and 4f–4f transition of trivalent praseodymium ions. The broad band in the range of 225–275 nm is attributed to inter-configurational 4f–5d transition. The peaks at 443, 459, and 488 nm (displayed in the inset of Fig. 5a) are ascribed to $^3H_4 \rightarrow {}^3P_2$, $^3H_4 \rightarrow {}^3P_1$, and $^3H_4 \rightarrow {}^3P_0$ f → f transitions of the Pr^{3+} ions, respectively. Very little change in the spectra could be seen as a function of the dopant concentration.

Pr^{3+} ions have two possible transitions, *i.e.* the La-Porte forbidden intra-configurational 4f–4f transitions and the allowed 4f–5d inter-configurational transitions.[48] The emission spectra of the $La_2Hf_2O_7$:*x*%Pr^{3+} NPs under excitation at 255 nm is shown in Fig. 4b. The emission spectra at various Pr^{3+} concentrations display the same spectral features. The peaks at 490, 534, 632, 662, and 727 nm correspond to the $^3P_0$–$^3H_4$, $^3P_0$–$^3H_5$, $^3H_5$, $^3P_0$–$^3F_2$, and $^3P_0$–$^3F_3$ transitions of Pr^{3+}, respectively. The emission peak at around 603 nm is attributed to $^1D_2$–$^3H_4$ transitions. Normally visible-light emission from the 4f → 4f transition of Pr^{3+} doped inorganic hosts is mostly seen from the $^3P_0$ and $^1D_2$ states. Based on the strength of the crystal field a host lattice offers, there may be variation in the relative intensity of the emission from these two states since the crystal field of the matrix materials determines where the bottom of the $4f^5d$ level of Pr^{3+} is going to lie with respect to the $^3P_0$ and $^1D_2$ states.[49] Whether the emission comes from the $^3P_0$ state or $^1D_2$ state or from both of them completely depends on the kind of host. Our literature survey shows that only green emission from $^3P_0$ can be seen in $CaZrO_3$ perovskite[50] whereas Pr^{3+}-doping displayed only red emission from the $^1D_2$ states in RE_2O_3 (RE = Sc, Y, and Gd) and Lu_2O_3.[51,52]

The relative intensities of the emissions from the $^3P_0$ and $^1D_2$ states depends on various photophysical phenomena, such as multi-phonon relaxation, cross-relaxation, intersystem crossing (ISC) through low-lying $4f^15d^1$ levels, and the charge transfer (CT) mechanism.[53] The nature of the host plays a key role as well in deciding the intensity ratio of the blue/green and red emissions from the $^3P_0$ and $^1D_2$ states, respectively, as the position of the charge transfer state (CTS) is dependent on the same. For the oxide-based host, it is normally localized around the excited states of the lanthanide ion.[54] Emission quenching from the $^3P_0$ state of the Pr^{3+} ions depends on the spectral position of the CTS with respect to the $^3P_0$ and $^1D_2$ states.[54] It is reported that the blue/green emission is more intense than the red emission in $CaTiO_3$, whereas the red emission is more intense than the green emission in $Na_5La(WO_4)_4$, $Na_5Y(WO_4)_4$, $CaTa_2O_6$, and $La_2Ti_2O_7$, and the $Gd_2Ti_2O_7$ type pyrochlore structure.[52,54,55] Our $La_2Hf_2O_7$:Pr^{3+} NPs can emit both intense green-blue ($^3P_0 \rightarrow {}^3H_4$) and red ($^1D_2 \rightarrow {}^3H_4$) emissions, which are important for inorganic phosphors. It seems replacing Ti^{4+} with Hf^{4+} in the pyrochlore structure changes the green to red ratio due to the difference in the crystal field induced by the HfO_6 octahedra when compared to TiO_6. The $La_2Hf_2O_6$ pyrochlore has two cationic sites, 8-coordinated La^{3+} (scalenohedra) and 6-coordinated Hf^{4+} sites (octahedra). In our $La_2Hf_2O_7$:Pr^{3+} NPs the origin of the emission from both the $^3P_0$ and $^1D_2$ states is attributed to the stabilization of Pr at both lanthanum sites as well as the Hf^{4+} site. For divalent and trivalent lanthanide ions, the difference in energy between the 4f 5d and 4f states is inversely proportional to the crystal field strength of the host matrix, which in turn increases as the distance between the lanthanide ion and the ligand decreases.[49] Since the La–O bond (0.264 nm) is longer than the Hf–O bond (0.208 nm), the effect of the ligand on the Pr^{3+} ion at the lanthanum site will be less when compared to that at the Hf site. Therefore, the emission from the $^3P_0$ level arises because of a fraction of the Pr^{3+} ions localized at the Hf^{4+} sites whereas the emission from the $^1D_2$ level arises due to the remaining Pr^{3+} ions being stabilized at the La^{3+} sites, however, the stabilization of Pr^{3+} at the Hf^{4+}

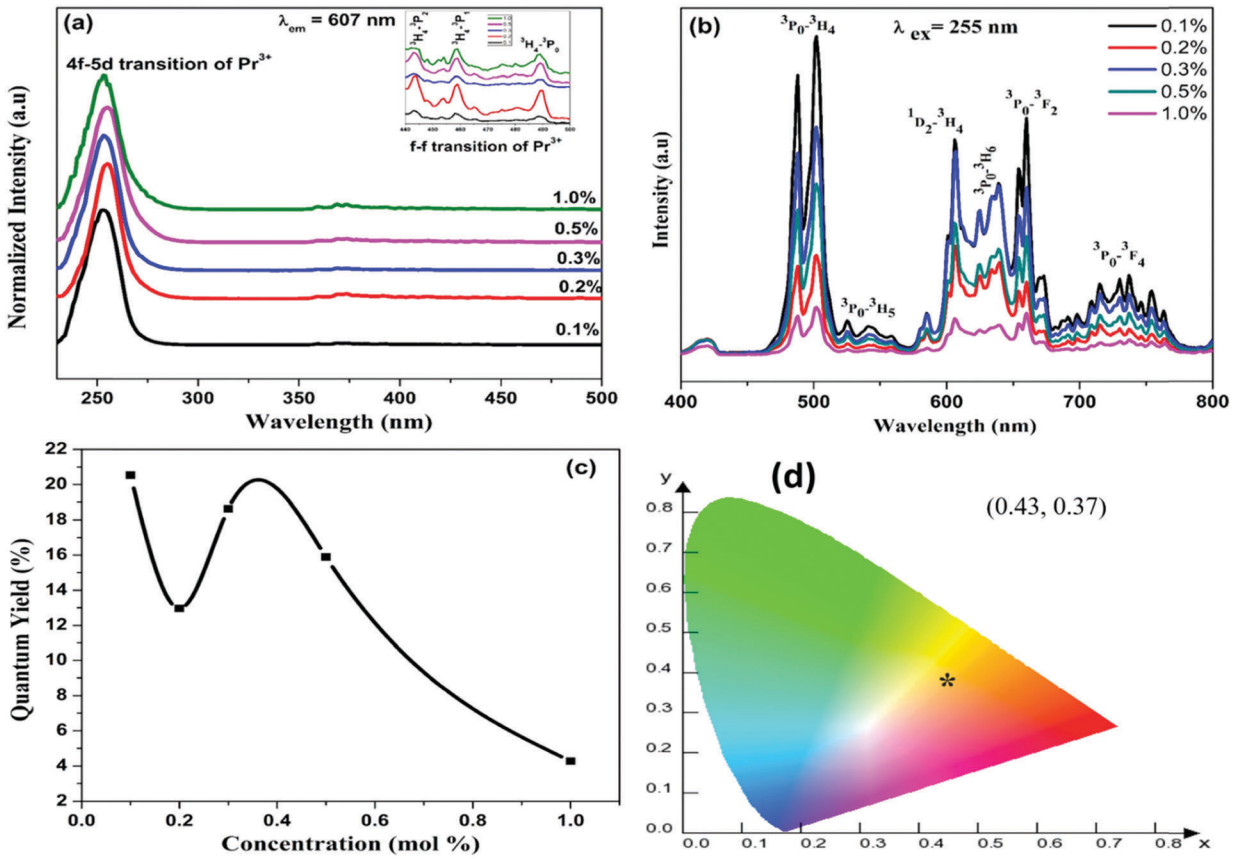

Fig. 4 The (a) excitation and (b) emission spectra, and (c) quantum yield as a function of the Pr^{3+}-doping concentration of the $La_2Hf_2O_7$:x%Pr^{3+} (x = 0.1, 0.2, 0.3, 0.5, and 1.0) NPs. (d) The CIE color coordinate diagram of the $La_2Hf_2O_7$:0.1%Pr^{3+} NPs.

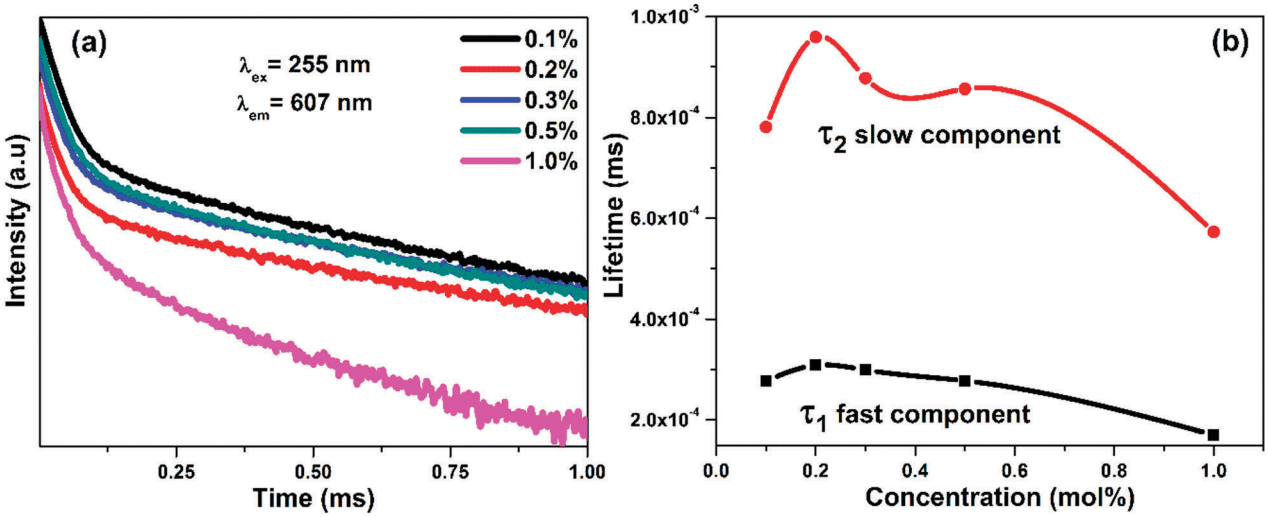

Fig. 5 (a) The luminescence decay profiles and (b) variation in the luminescence lifetimes of the $La_2Hf_2O_7$:$x$mol%Pr^{3+} (x = 0.1, 0.2, 0.3, 0.5, and 1.0) NPs at λ_{ex} = 255 nm and λ_{em} = 607 nm.

sites may leads to the generation of a large concentration of oxygen vacancies.[21]

The quantum yields were determined using an integrating sphere in our FLS 980 system and the results shown in Fig. 4c. The $La_2Hf_2O_7$:0.1%Pr^{3+} NPs were found to possess the strongest emission intensity with a quantum yield (QY) of 20.54 ± 0.1%. Beyond the 0.1%Pr^{3+}-doping level, the emission intensity and QY were found to decrease, which is attributed to concentration quenching. The problem of concentration induced fluorescence quenching even at low Pr^{3+} concentrations is a well-known

issue even though efficient luminescence in phosphors doped with high concentrations of Pr^{3+} have been reported.[56] The concentration quenching is attributed to non-radiative energy transfer (ET) between two Pr^{3+} ions at high concentrations when they are at a closed distance known as the critical distance. Non-radiation transition arises mainly because cross-relaxation ET from one Pr^{3+} ion to another. Based on the Pr^{3+} energy level diagram, the difference in energy between the $^3P_0$ and $^3H_6$ states is approximately around 16 000 cm^{-1}, and that between the $^3H_4$ and $^1D_2$ level is close to 16 700 cm^{-1}.[48,57] Concentration quenching in this case is mainly induced by the cross-relaxation process between neighboring Pr^{3+} ions.[58] Based on the critical distance, one can predict the mechanism of concentration quenching.

The colorimetric performance of the $La_2Hf_2O_7$:0.1mol%Pr^{3+} NPs, *i.e.* the NPs with the maximum emission output and QY, was established using the color-coordinates calculated using the intensity-corrected emission spectra excited at 255 nm with respect to the monochromator, source and detector. The calculated CIE color-coordinates obtained for the $La_2Hf_2O_7$:0.1%Pr^{3+} NPs were found to be 0.433 and 0.370, which are located in the color-coordinated CIE diagram and confirm the red-yellow emission from the Pr^{3+} doped lanthanum hafnate NPs (on the boundary line of the CIE white domain), as shown in Fig. 4d. With respect to the previous emission profile (Fig. 5b) and proceeding radioluminescence data (Fig. 6 and 7), both optical tests agree with the quantum yield results proving the 0.1%Pr^{3+} doped $La_2Hf_2O_7$ sample was the most efficient one among all our samples.

The lifetime studies of the $^1D_2 \rightarrow {}^3H_4$ transition (607 nm) of Pr^{3+} ions in the $La_2Hf_2O_7$:*x*%Pr^{3+} NPs were performed using a pulsed Xenon lamp with excitation at 255 nm, as shown in Fig. 5a. The decay profiles displayed non-exponential behavior, however, the $^1D_2$ level decays by three different processes: radiative decay ($^1D_2 \rightarrow {}^3H_4$), multi-photon relaxation ($^1D_2 \rightarrow {}^1G_2$), and cross-relaxation induced energy transfer ($^1D_2 \rightarrow {}^3H_4/{}^3H_4 \rightarrow {}^3F_{3,4}$).[54] This non-exponential behavior is mainly due to cross-relaxation and luminescence quenching. Cross-relaxation is a photophysical phenomenon wherein the excitation energy from an ion decaying from a highly excited state promotes a nearby ion from the ground state to a metastable level. In this case, the non-exponential decay profiles were fitted using a bi-exponential equation:

$$I(t) = A_0 + A_1 \exp\left(\frac{-t}{\tau_1}\right) + A_2 \exp\left(\frac{-t}{\tau_2}\right)$$

where $I(t)$ is PL intensity, τ_1 and τ_2 are emission decay times, and A_1 and A_2 are their relative weightages. Table 2 shows two lifetime values observed for Pr^{3+} in the order of 170–310 μs (T_S, short lifetime) and 570–960 μs (T_L, longer lifetime). As a function of the dopant concentration both the lifetime values

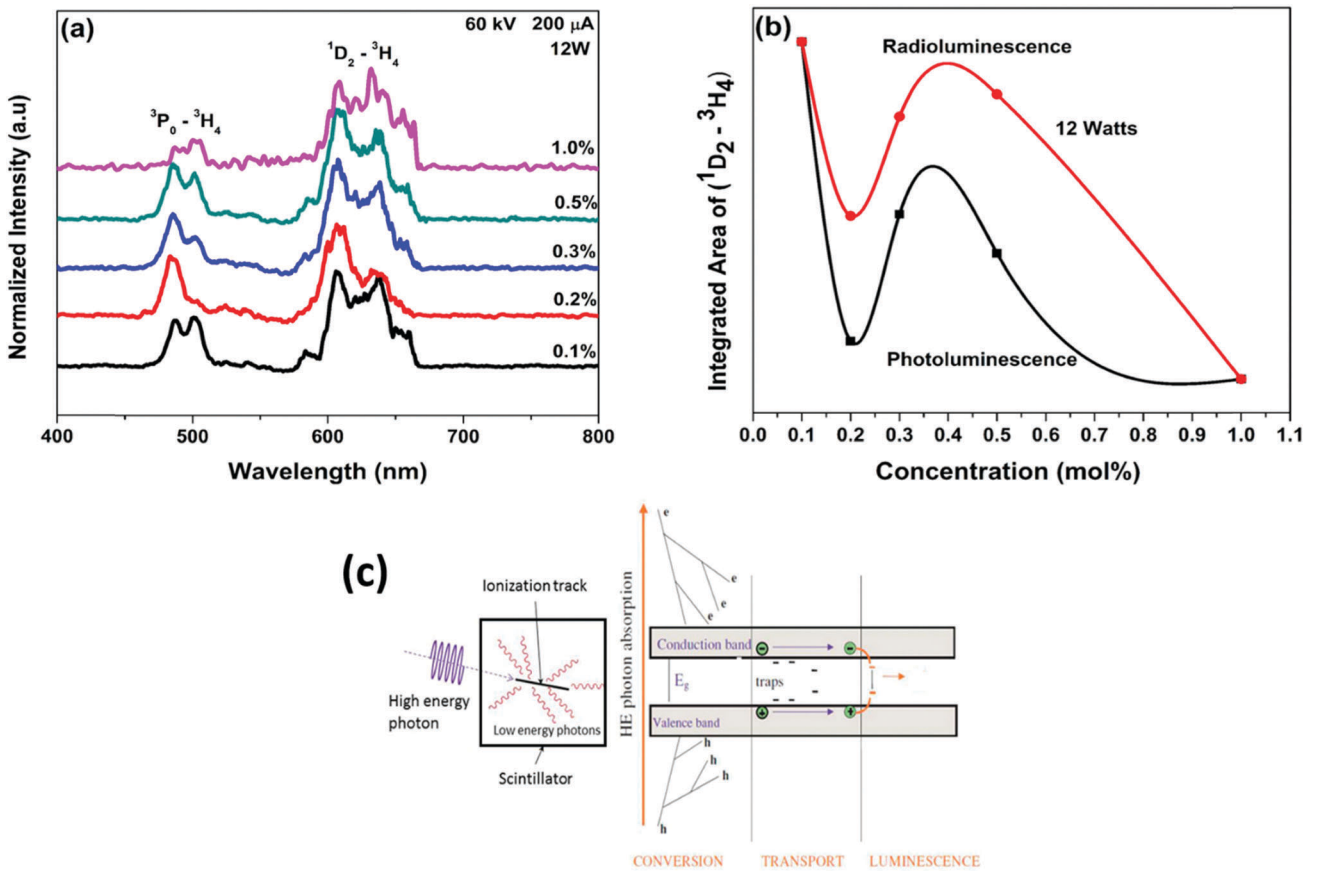

Fig. 6 The (a) XEL spectra and (b) a comparison of the concentration dependence of the XEL and PL intensities as a function of dopant concentration of the $La_2Hf_2O_7$:*x*%Pr^{3+} NPs. (c) The scintillation mechanism for doped materials.

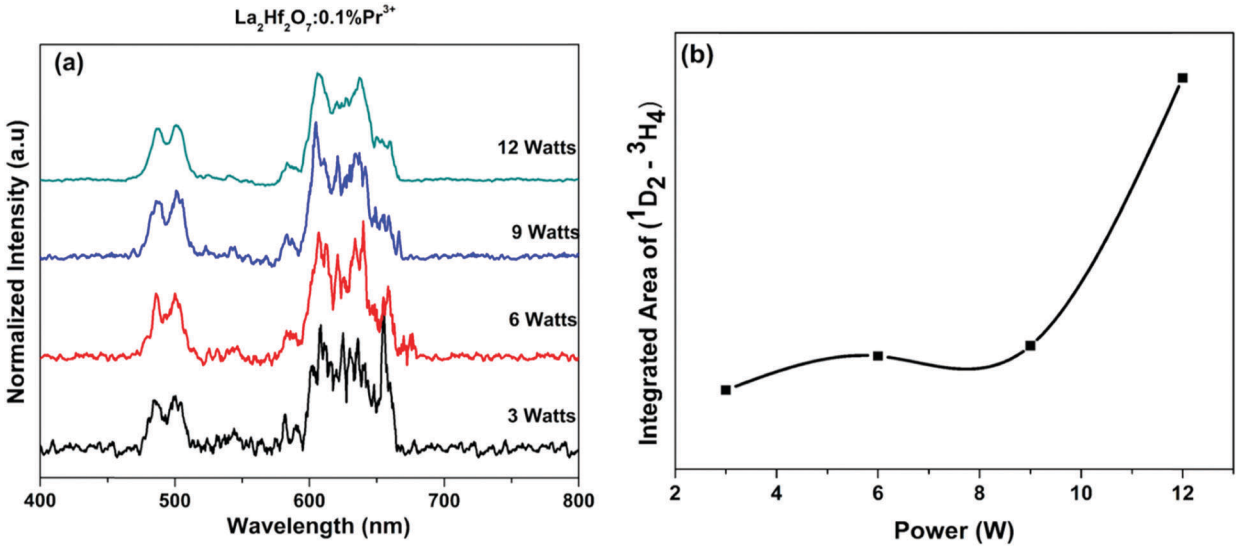

Fig. 7 The (a) XEL spectra and (b) variation in the emission output from the $^3P_0 \rightarrow {}^3H_4$ transition of Pr^{3+} ions in the $La_2Hf_2O_7$:0.1%Pr^{3+} NPs at various X-ray powers.

Table 2 The luminescence lifetime data obtained for the $La_2Hf_2O_7$:x mol%Pr^{3+} NPs (λ_{ex} = 255 nm and λ_{em} = 607 nm) at various dopant ion concentrations (x = 0.1, 0.2, 0.3, 0.5, and 1.0)

Pr^{3+} doping concentration (%)	τ_1 (μs)	τ_2 (μs)
0.10	277.2	781.3
0.20	308.3	959.1
0.30	299.1	877.6
0.50	277.5	856.7
1.00	170.0	572.8

initially increase upon increasing the Pr^{3+} ion concentration up to 0.2 mol%, but beyond that dopant level, the lifetime values start to decrease (Fig. 5b). In most of the literature studies on Pr^{3+}-doped phosphor materials, the lifetime values are in the range of nanoseconds to 50 μs. In our case, the lifetime values are exceedingly high. The average value is 814 μs for the $La_2Hf_2O_7$: 0.2mol%Pr^{3+} NPs.[59] This suggests that the Pr^{3+} ions are not homogenously distributed in the $La_2Hf_2O_7$ host. When the activator ions have different local sites, they are likely to relax at different transition rates. If the rates of relaxations are very distinct, then different decays co-exist for the activator ions. Assuming a given phonon energy occurs because the Pr^{3+} ions are localized in the same $La_2Hf_2O_7$ host, the relatively longer lived Pr^{3+} ions (570–960 μs) are ascribed to a relatively symmetrical site/environment as the 4f–4f transition are optically forbidden in sites with inversion symmetry, whereas the short-lived Pr^{3+} ions (170–310 μs) are more likely to arise from those occupying an asymmetric site, wherein the selection rules are relaxed. In $La_2Hf_2O_7$ pyrochlore, the Pr^{3+} ions are more likely to be stabilized at two sites: The symmetric La^{3+} site (S1) with regular LaO_8 polyhedral and the relatively asymmetric Hf^{4+} site (S2) with HfO_6 distorted octahedral. Fast decaying species (170–310 μs) T_S arise because of the Pr^{3+} ions occupying the Hf^{4+} (S2) site without inversion symmetry, whereas slow decaying species T_L can be attributed to the Pr^{3+} ions occupying the La^{3+} (S1) site with inversion symmetry. Such site selective luminescence spectroscopy for rare earth ions (Eu, Sm, Dy, and Tb) has been reported in many hosts.[59–64] However, we cannot rule out the contribution of cross-relaxation and fluorescence quenching on this phosphor for the non-exponential decay.

3.7 Radioluminescence: optical properties under X-ray excitation

The $La_2Hf_2O_7$:x%Pr^{3+} NPs have an interesting lattice for scintillators. Considering the high density (7.8 gm cm^{-3}) and the potential of lanthanum hafnate materials as a scintillator,[21] the X-ray exited luminescence (XEL) spectra were recorded for these NPs. As shown in Fig. 6a, the XEL spectra look very similar to the photon VUV and UV excited luminescence spectra. In addition, there was not much change as a function of the dopant concentration. The marginal variation can be ascribed to the sensitivity of the PMT used. The RL emission spectra (Fig. 6a) display the typical characteristics of Pr^{3+} ions with peak positions similar to those seen in the photoluminescence spectra (Fig. 4b). As such, X-ray excitation is different from UV excitation since under X-ray excitation e^-–h^+ pairs are generated and the Pr^{3+} 4f–5d/4f–4f bands and hosts are excited together. In this situation, e^- migrate to the Pr^{3+} centers whereas under UV, only the Pr^{3+} (4f–5d/4f–4f) bands are excited but not the host. As discussed, the Pr^{3+} ions are distributed at both the La^{3+} and Hf^{4+} sites in lanthanum hafnate. For $La_2Hf_2O_7$, the valence band (VB) is composed of O 2p orbitals hybridized with the Hf 5d orbitals along with a minor contribution from the La 4f states. On the other hand, the conduction band (CB) is mainly composed of La 4d states (in majority spin component), 4f states (in minority spin component) and Hf 5d states. The Hf 5d states contribute solely to the lower part of the conduction band.[65] The Pr^{3+} ions occupying the tetravalent hafnium sites may lead to a negative antisite defect $\left(Pr'_{Hf}\right)$ as well as a positive defect $\left(V_O^{\bullet\bullet}\right)$ as indicated below.

$$Pr^{3+} + Hf^{4+} \rightarrow Pr'_{Hf} + V_O^{\bullet\bullet}$$

Moreover, this Pr'_{Hf} defect is XEL active and amenable to emission under X-ray excitation. This is similar to what Dobrowolska *et al.* observed in barium hafnate doped with europium ions.[66] Excitation with a 12 W energetic X-ray beam leads to the formation of an exciton (bound electron–hole pair) between an electron in the lower part of the CB comprised of the Hf 5d states ($5d^1$ Hf^{3+}) and a hole in the VB if they possess similar momentum. The next step is transfer of the excitons energy to the Pr'_{Hf} luminescent center followed by the emission of the luminescent ions that radiatively return from an excited state to the ground state. The XEL arises from both the $^3P_0$ and $^1D_2$ states around 472–512 nm ($^3P_0 \rightarrow {}^3H_4$) and 595–635 nm ($^1D_2 \rightarrow {}^3H_4$), respectively. The dependence of the XEL intensity on the dopant concentration follows a similar trend as the PL, and the highest intensity was found to be at a 0.1% doping level (Fig. 6b). The PL and XEL emission profile look quite similar, which indicates the same radiative levels, are involved in the emission in the visible-light region in both cases.

Looking out for Pr^{3+}-activated oxide based phosphor materials and their application as scintillators for X-ray computed tomography requires chemical modifications, which need the fast decaying $^3P_0 \rightarrow {}^3H_4$ transition (in μs range) to be more intense than the slow decaying $^1D_2 \rightarrow {}^3H_4$ transition (in ms range). On the other side, solid-state lighting applications require the dominance of the $^1D_2 \rightarrow {}^3H_4$ emission over that of the $^3P_0 \rightarrow {}^3H_4$ transition. Herein, we could get emission from both states though the red emission from the $^1D_2$ states being more dominant than the $^3P_0$ state in our samples. The larger fraction of the $^1D_2$ state in our XEL spectra is not very advantageous as it has a much longer decay time. From the XEL spectrum we can decipher that lanthanum hafnate activated with Pr^{3+} ions can convert the incoming high energy X-ray photon into visible-light. The mechanism of the XEL is depicted in Fig. 6c. In the present case, though the XEL efficiency is rather low, our results are still encouraging enough to give a direction wherein we could modify the pyrochlore lattice to enhance the emission from the $^3P_0$ states. This is connected with the nature of the Wannier–Mott type excitons in $La_2Hf_2O_7$, which exist for oxides with a high dielectric constant.[67,68] They are weakly bound and have large radii that are known as large excitons and as a result, on collision with phonons they are easily destructed.[66] Because of this, the number of excitons formed during X-ray excitation in the case of $La_2Hf_2O_7$:Pr^{3+} is relatively lower in magnitude than that in materials where Frenkel-type excitons are formed. The exciton–exciton interactions are less probable due to their lower mobility, which results in a lower probability for energy transfer and a lower luminescence intensity.

Lastly, a X-ray dosage dependence study was conducted to determine the best emission output with respect to the power (Fig. 7a). The $La_2Hf_2O_7$:0.1%Pr^{3+} NPs were used in this study due to its outstanding emission performance over the other samples. This is important to understand because it allows one to differentiate the durability and performance when exposed at different powers of radiation. It was found that the maximum emission output was acquired at 12 W (Fig. 7b).

Furthermore, $La_2Hf_2O_7$ is a material with a high dielectric constant and the excitons formed in these cases on exposure to ionizing radiation such as X-ray are weakly bound, known as Wannier–Mott type excitons (WMEs). They break easily on collision with phonons. The number of excitons thus available for energy transfer to Pr^{3+} ions will be less and hence, a low RL output as shown in Fig. 6a and 7a. On the other hand, under UV excitation at 255 nm, the $La_2Hf_2O_7$ host absorbs the energy and transfer to radiative Pr^{3+} centers directly. This is known as host sensitized energy transfer. This is why the emitted photon counts corresponding to the green and red emissions under the UV excitation (Fig. 4b) are larger than the ones excited by X-rays.

4. Conclusions

In this study, $La_2Hf_2O_7$:*x*mol%Pr^{3+} NPs (x = 0, 0.1, 0.2, 0.3, 0.5, and 1.0) were synthesized using a molten salt synthesis and systematically characterized using XRD, Raman and FTIR spectroscopy, XPS, SEM, TEM and UV/X-ray-excited optical luminescence. Raman spectroscopy confirmed the structure of the $La_2Hf_2O_7$ NPs to be the ordered pyrochlore while XPS reflected the formation of oxygen vacancies due to the stabilization of a fraction of the Pr^{3+} ions at the Hf^{4+} sites. The presence of La–O and Hf–O vibration bonds was confirmed through FTIR spectroscopy. The spherical shape of the NPs was confirmed by SEM and TEM, which also confirmed the formation of $La_2Hf_2O_7$:Pr^{3+} nanodomains. The photoluminescence data reveal the presence of green and red emissions due to the $^3P_0 \rightarrow {}^3H_4$ and $^1D_2 \rightarrow {}^3H_4$ transitions. However, the emission from the $^1D_2$ states was found to be more intense than those from the $^3P_0$ states. This phenomenon has a huge implication in the design of novel phosphors for possible applications in solid-state lighting. The colorimetric performance of the $La_2Hf_2O_7$:0.1mol%Pr^{3+} NPs confirmed the red-yellow emission from the $^3P_0$ level due to the Pr^{3+} ions localized at the Hf^{4+} sites. On the other hand, emission from the $^1D_2$ states arises from the Pr^{3+} localized at the La^{3+} sites. In addition, the $La_2Hf_2O_7$:0.1mol%Pr^{3+} NPs were found to possess the strongest emission intensity with a quantum yield of 20.54 ± 0.1%. However, beyond the 0.1%Pr^{3+}-doping level, the emission intensity and QY of the $La_2Hf_2O_7$:*x*%Pr^{3+} NPs were found to decrease, which is attributed to concentration quenching. Lifetime spectroscopy confirmed that the fast decay in the range of 170–310 μs arises because some Pr^{3+} ions occupy the Hf^{4+} sites whereas the slow decay in the range of 570–960 μs can be attributed to Pr^{3+} ions occupying the La^{3+} sites. X-ray induced optical luminescence displayed the intense green and red emissions arising from the $^3P_0$ and $^1D_2$ states of the Pr^{3+} ions. The effect of changing the X-ray power on the radioluminescence was also explored and we could see the intensity was monotonically increased as a function of the X-ray power. All together, we have developed and investigated a series of $La_2Hf_2O_7$:*x*mol%Pr^{3+} NPs in this work with exciting results not only for luminescence applications but also opening a new gateway for doped pyrochlores NPs in scintillator applications.

Conflicts of interest

There are no conflicts to declare.

Acknowledgements

The authors thank the financial support by the National Science Foundation under CHE (Award #1710160) and DMR (Grant #1523577), and the USDA National Institute of Food and Agriculture (Award #2015-38422-24059, for the Integrating Food Science/Engineering and Education Network (IFSEEN) program). The Department of Chemistry at the University of Texas Rio Grande Valley is grateful for the generous support provided by a Departmental Grant from the Robert A. Welch Foundation (Grant No. BX-0048). SKG would like to thank the United States-India Education Foundation (USIEF) and Institute of International Education (IIE) for his Fulbright Nehru Postdoctoral Fellowship (Award #2268/FNPDR/2017).

References

1 M. Shang, S. Liang, N. Qu, H. Lian and J. Lin, *Chem. Mater.*, 2017, **29**, 1813–1829.
2 S. Li, D. Tang, Z. Tian, X. Liu, T. Takeda, N. Hirosaki, F. Xu, Z. Huang and R.-J. Xie, *J. Mater. Chem. C*, 2017, **5**, 1042–1051.
3 J. Xu, D. Murata, J. Ueda and S. Tanabe, *J. Mater. Chem. C*, 2016, **4**, 11096–11103.
4 V. Havasi, B. Vödrédi and Á. Kukovecz, *Catal. Today*, 2017, **284**, 107–113.
5 C. W. Kim, T. Y. Eom, I. S. Yang, B. S. Kim, W. I. Lee, Y. S. Kang and Y. S. Kang, *Sci. Rep.*, 2017, **7**, 6849.
6 G. F. Knoll, *Radiation detection and measurement*, John Wiley & Sons, 2010.
7 A. Kamkaew, F. Chen, Y. Zhan, R. L. Majewski and W. Cai, *ACS Nano*, 2016, **10**, 3918–3935.
8 M. D. Birowosuto, D. Cortecchia, W. Drozdowski, K. Brylew, W. Lachmanski, A. Bruno and C. Soci, *Sci. Rep.*, 2016, **6**, 37254.
9 Y. Tsubota, J. H. Kaneko, M. Higuchi, S. Nishiyama and H. Ishibashi, *Appl. Phys. Express*, 2015, **8**, 062602.
10 P. Lecoq, *Nucl. Instrum. Methods Phys. Res., Sect. A*, 2016, **809**, 130–139.
11 G. Rooh, A. Khan, H. Kim, H. Park and S. Kim, *Opt. Mater.*, 2017, **73**, 523–526.
12 F. Zhong, J. Zhao, L. Shi, Y. Xiao, G. Cai, Y. Zheng and J. Long, *Sci. Rep.*, 2017, **7**, 4684.
13 S. Mahade, N. Curry, S. Björklund, N. Markocsan, P. Nylén and R. Vaßen, *Surf. Coat. Technol.*, 2017, **318**, 208–216.
14 M. Sun and B. Huang, *Inorg. Chem.*, 2017, **56**, 7975–7984.
15 M. T. Malachevsky, D. Rodríguez Salvador, S. Leiva and C. A. D'Ovidio, *J. Ceram.*, 2015, **2015**, 298690.
16 X. Shu, X. Lu, L. Fan, R. Yang, Y. Ding, S. Pan, P. Zhou and Y. Wu, *J. Mater. Sci.*, 2016, **51**, 5281–5289.
17 Y. Ji, D. Jiang, T. Fen and J. Shi, *Mater. Res. Bull.*, 2005, **40**, 553–559.
18 J. Trojan-Piegza, S. Gierlotka, E. Zych and W. Lojkowski, *J. Am. Ceram. Soc.*, 2014, **97**, 1595–1601.
19 K. Wahid, M. Pokhrel and Y. Mao, *J. Solid State Chem.*, 2017, **245**, 89–97.
20 R. A. Hansel, S. Desai, S. W. Allison, A. Heyes and D. G. Walker, *J. Appl. Phys.*, 2010, **107**, 016101.
21 M. Pokhrel, K. Wahid and Y. Mao, *J. Phys. Chem. C*, 2016, **120**, 14828–14839.
22 A. Srivastava, *J. Lumin.*, 2016, **169**, 445–449.
23 S. L. Cates, E. L. Cates, M. Cho and J.-H. Kim, *Environ. Sci. Technol.*, 2014, **48**, 2290–2297.
24 Y. Eagleman, M. Weber, A. Chaudhry and S. Derenzo, *J. Lumin.*, 2012, **132**, 2889–2896.
25 Y. Ji, D. Jiang and J. Shi, *J. Mater. Res.*, 2005, **20**, 567–570.
26 J. Trojan-Piegza, E. Zych and M. Kosińska, *Radiat. Meas.*, 2010, **45**, 432–434.
27 F. N. Sayed, V. Grover, K. Bhattacharyya, D. Jain, A. Arya, C. Pillai and A. Tyagi, *Inorg. Chem.*, 2011, **50**, 2354–2365.
28 M. Glerup, O. F. Nielsen and F. W. Poulsen, *J. Solid State Chem.*, 2001, **160**, 25–32.
29 M. Li, D. Zhou, C. P. Li and Z. Zhao, *Mater. Sci. Semicond. Process.*, 2016, **44**, 101–107.
30 I. E. Seferis and E. Zych, *J. Lumin.*, 2016, **169**, 838–843.
31 Y. Mao, X. Guo, J. Y. Huang, K. L. Wang and J. P. Chang, *J. Phys. Chem. C*, 2009, **113**, 1204–1208.
32 Y. Mao, T. J. Park, F. Zhang, H. Zhou and S. S. Wong, *Small*, 2007, **3**, 1122–1139.
33 E. Gilardi, E. Fabbri, L. Bi, J. L. Rupp, T. Lippert, D. Pergolesi and E. Traversa, *J. Phys. Chem. C*, 2017, **121**, 9739–9747.
34 T. M. H. Nguyen, L. J. Sandilands, C. Sohn, C. Kim, A. L. Wysocki, I.-S. Yang, S. Moon, J.-H. Ko, J. Yamaura and Z. Hiroi, *Nat. Commun.*, 2017, **8**, 251.
35 K. M. Turner, D. R. Rittman, R. A. Heymach, C. L. Tracy, M. L. Turner, A. F. Fuentes, W. L. Mao and R. C. Ewing, *J. Phys.: Condens. Matter*, 2017, **29**, 255401.
36 N. Garg, K. Pandey, C. Murli, K. Shanavas, B. P. Mandal, A. Tyagi and S. M. Sharma, *Phys. Rev. B: Condens. Matter Mater. Phys.*, 2008, **77**, 214105.
37 P. E. Blanchard, S. Liu, B. J. Kennedy, C. D. Ling, M. Avdeev, J. B. Aitken, B. C. Cowie and A. Tadich, *J. Phys. Chem. C*, 2013, **117**, 2266–2273.
38 S. Mahesh, P. P. Rao, M. Thomas, T. L. Francis and P. Koshy, *Inorg. Chem.*, 2013, **52**, 13304–13313.
39 Z. Wang, H. Zhu, L. Ai, X. Liu, M. Lv, L. Wang, Z. Ma and Z. Zhang, *J. Colloid Interface Sci.*, 2016, **478**, 209–216.
40 D. A. Pawlak, M. Ito, M. Oku, K. Shimamura and T. Fukuda, *J. Phys. Chem. B*, 2002, **106**, 504–507.
41 M. Sunding, K. Hadidi, S. Diplas, O. Løvvik, T. Norby and A. Gunnæs, *J. Electron Spectrosc. Relat. Phenom.*, 2011, **184**, 399–409.
42 Q.-H. Wu, M. Liu and W. Jaegermann, *Mater. Lett.*, 2005, **59**, 1980–1983.
43 T.-M. Pan, F.-H. Chen and Y.-H. Shao, *RSC Adv.*, 2015, **5**, 51286–51289.
44 S. Rudenja, A. Minko and D. Buchanan, *Appl. Surf. Sci.*, 2010, **257**, 17–21.

45 H. Xie, Q. Liu, Y. Li, H. Lv, M. Wang, X. Liu, H. Sun, X. Yang, S. Long and S. Liu, *Semicond. Sci. Technol.*, 2012, **27**, 125008.
46 K. Bomben, J. Moulder, P. Sobol and W. Stickle, *Physical Electronics*, Eden Prairie, MN, 1995.
47 M. Pokhrel, M. Alcoutlabi and Y. Mao, *J. Alloys Compd.*, 2017, **693**, 719–729.
48 A. A. Kaminskii, *Laser Crystals: Their Physics and Properties*, Springer, 2013.
49 S. N. Ogugua, H. C. Swart and O. M. Ntwaeaborwa, *Sens. Actuators, B*, 2017, **250**, 285–299.
50 H. Hoefdraad and G. Blasse, *Phys. Status Solidi A*, 1975, **29**, K95–K97.
51 C. D. M. Donega, A. Meijerink and G. Blasse, *J. Phys. Chem. Solids*, 1995, **56**, 673–685.
52 G. Aumüller, W. Köstler, B. Grabmaier and R. Frey, *J. Phys. Chem. Solids*, 1994, **55**, 767–772.
53 P. Boutinaud, E. Pinel, M. Oubaha, R. Mahiou, E. Cavalli and M. Bettinelli, *Opt. Mater.*, 2006, **28**, 9–13.
54 K. Jaroszewski, M. Chrunik, P. Głuchowski, E. Coy, B. Maciejewska, R. Jastrzab, A. Majchrowski and D. Kasprowicz, *Opt. Mater.*, 2016, **62**, 72–79.
55 L. Noto, M. Chithambo, O. Ntwaeaborwa and H. Swart, *J. Alloys Compd.*, 2014, **589**, 88–93.
56 Y. Guan, T. Tsuboi, Y. Huang and W. Huang, *Dalton Trans.*, 2014, **43**, 3698–3703.
57 F. Chun, B. Zhang, H. Su, H. Osman, W. Deng, W. Deng, H. Zhang, X. Zhao and W. Yang, *J. Lumin.*, 2017, **190**, 69–75.
58 H. Dornauf and J. Heber, *J. Lumin.*, 1980, **22**, 1–16.
59 B. Liu, J. Shi, Q. Wang, H. Tang, J. Liu, H. Zhao, D. Li, J. Liu, X. Xu and Z. Wang, *J. Lumin.*, 2018, **196**, 76–80.
60 S. K. Gupta, P. Ghosh, N. Pathak, A. Arya and V. Natarajan, *RSC Adv.*, 2014, **4**, 29202–29215.
61 S. K. Gupta, P. S. Ghosh, A. K. Yadav, S. N. Jha, D. Bhattacharyya and R. M. Kadam, *Inorg. Chem.*, 2016, **56**, 167–178.
62 S. K. Gupta, P. S. Ghosh, A. K. Yadav, N. Pathak, A. Arya, S. N. Jha, D. Bhattacharyya and R. M. Kadam, *Inorg. Chem.*, 2016, **55**, 1728–1740.
63 S. K. Gupta, S. Nigam, A. K. Yadav, M. Mohapatra, S. N. Jha, C. Majumder and D. Bhattacharyya, *New J. Chem.*, 2015, **39**, 6531–6539.
64 S. K. Gupta, M. Sahu, K. Krishnan, M. Saxena, V. Natarajan and S. Godbole, *J. Mater. Chem. C*, 2013, **1**, 7054–7063.
65 N. Li, H. Xiao, X. T. Zu, L. M. Wang, R. C. Ewing, J. Lian and F. Gao, *J. Appl. Phys.*, 2007, **102**, 063704.
66 A. Dobrowolska and E. Zych, *J. Lumin.*, 2017, **192**, 397–403.
67 G. H. Wannier, *Phys. Rev.*, 1937, **52**, 191.
68 D. Liu, K. Tse and J. Robertson, *Appl. Phys. Lett.*, 2007, **90**, 062901.

